applied sciences

MDPI

Article

Erosion Rate Measurements for DART Spacecraft Ion Propulsion System †

Mark W. Crofton [1,*], Donner T. Schoeffler [1,2], Jason A. Young [1] and Michael J. Patterson [3,4,*]

[1] Propulsion Science Department, The Aerospace Corporation, El Segundo, CA 90245, USA
[2] Graduate Aerospace Laboratories, California Institute of Technology, Pasadena, CA 91125, USA
[3] NASA Glenn Research Center, Cleveland, OH 44135, USA
[4] Desert Works Propulsion, Carrizozo, NM 88301, USA
* Correspondence: mark.w.crofton@aero.org (M.W.C.); mjpatterson@desertworkspropulsion.com (M.J.P.)
† This paper is an extended version of paper published in AIAA SciTech Forum, held in San Diego, CA, USA, 7–11 January 2019.

Featured Application: Evaluation of real-time erosion characteristics of the NEXT ion engine under simulated flight conditions for the DART planetary defense mission, using a laser probe.

Abstract: The Double Asteroid Redirection Test (DART) spacecraft was developed to provide the first measurement for orbital deflection of an asteroid upon intentional impact. The NEXT ion engine is part of the mission, on its maiden voyage. As part of the pre-launch risk reduction, erosion characteristics of the extraction grid system were evaluated using laser measurements of sputtered molybdenum atoms over the envelope of potential throttle conditions for the mission. Erosion rate dependence on propellant flow rate as well as relative density and directionality of molybdenum sputter from grid center to edge were measured. Sputtered atoms were found to have average radial velocity directed toward the engine perimeter and increasing with radial distance. The relative contribution of source and facility background gas and other sources of accelerator grid current was examined as well as the influence of several engine operating parameters. Facility background gas was found to influence engine operation more than a wall-mounted pressure gauge and typical assumptions about ingestion would indicate. Far-field flux was estimated over the full angular range based on the near-field relative density and velocity results and relying on quartz crystal microbalance data at one location to fix absolute numbers everywhere. The results substantially deepen knowledge and understanding of the complex grid erosion process of the engine and its lifetime, as grid failure via erosion is the normal life limiter. Study results are also relevant to thruster–spacecraft integration issues such as molybdenum deposition rate on solar cells and other spacecraft surfaces.

Keywords: laser; plasma; ion engine; accelerator grid; DART; asteroid; erosion; molybdenum; ion propulsion

Citation: Crofton, M.W.; Schoeffler, D.T.; Young, J.A.; Patterson, M.J. Erosion Rate Measurements for DART Spacecraft Ion Propulsion System. *Appl. Sci.* **2022**, *12*, 7831. https://doi.org/10.3390/app12157831

Academic Editor: Jérôme Morio

Received: 7 June 2022
Accepted: 18 July 2022
Published: 4 August 2022

1. Introduction

The Double Asteroid Redirection Test (DART) is the world's first planetary defense test mission [1,2]. It is intended to measure orbital deflection of an asteroid upon intentional impact. The DART spacecraft includes several advanced technologies for demonstration, among them the NEXT (NASA's Evolutionary Xenon Thruster) ion engine [3] on its maiden flight. Due to favorable circumstances of the DART launch in November 2021, augmentation of the Didymos B asteroid impact velocity by NEXT was very modest—much less than previously planned. NEXT extracts xenon ions through thousands of individual grid aperture pairs, forming ion beamlets that combine to make a macroscopic ion beam. These engines sputter grid material into the plume, potentially shortening the thruster lifetime [3–5]. Despite substantially higher grid lifetime compared to previous ion engine

designs, the primary failure mechanism is still expected to result from degradation of the accelerator grid structure by ion sputtering effects. Plume sputter flux depends on distance and angle, thruster operating point, grid material, and facility background pressure. Net mass deposition rates are also a function of ion beam flux profile, due to competition between deposition and erosion rates. Ion beam flux varies much more strongly with plume angle than molybdenum flux. Absolute measurements of real-time net mass deposition rate for surfaces exposed to the plume of a NASA NEXT ion engine with molybdenum grids have been previously performed [6]. Although NEXT had been characterized in considerable detail previously, data were lacking for engine operation over the range of potential flow rate conditions for the DART mission. Flow conditions deviate from standard throttle table settings established in ground tests due to reduced flow system accuracy for the flight configuration. The flow of interest is the total passing through the discharge chamber, which is the sum of discharge cathode (DCA) and main chamber rates. For the present study, the flow rate dependence of thruster extraction grid erosion was investigated, varying the flow rate about the standard operating condition targeted for DART.

In addition to effects on thruster lifetime, erosion and deposition effects lead directly to integration issues for the spacecraft that use them. Metal and insulator atoms and ions produced via sputter erosion may find their way into the plume and deposit on spacecraft surfaces, modifying their properties. Due to the inherent divergence of the ion beam, there may be intercepted spacecraft surfaces that undergo sputter erosion, modifying roughness, composition, and thickness, and other surfaces with net deposition that leads to modified thermal, optical, and electrical properties. Erosion and deposition processes inside thrusters may modify lifetime potential of the device, and facility effects can create a difference between ground test and in-space operation and lifetime.

Ion engine grids are typically fabricated from molybdenum. This is the case for NSTAR, XIPS, and NEXT ion engines. Other materials, especially titanium and pyrolytic graphite (carbon) grids, are replacement candidates. NASA's NEXT ion engine has a relatively low grid sputter rate and long lifetime [3]. Because molybdenum plume density is approximately proportional to wear rate, for a given geometry, the low erosion rate of NEXT limits its molybdenum plume density and makes in situ detection more challenging. NEXT was designed with two extraction grids: screen and accelerator. Erosion occurs primarily on the accelerator grid, due to xenon ion impingement. Age of the grids is a factor, and operating hours were relatively low in the present case. Erosion rate can be studied by various techniques, including real-time imaging of grid apertures, post-test dimensional measurements, and real-time monitoring of erosion/deposition products. Fixed position and rotating quartz crystal microbalances (QCMs) were used previously to study plume deposition rates for NEXT [6], and laser induced fluorescence (LIF) was also utilized [7]. Real-time monitoring of plume molybdenum density via LIF or deposition via QCM can be challenging from a detection standpoint. The interpretation of witness plate and QCM data is more complex if molybdenum arrival rate is low, due to surface reactions with residual gas. The back-sputter of carbon from facility walls to thruster grids will alter their erosion rate if carbon deposition is fast enough. Carbon back-sputter has been measured previously and its effect analyzed [8,9].

For the present study, previously described in a conference paper [10], LIF Doppler profiles were obtained across the grid face for several DART operating points, and the effect of flow variation over the envelope possible for DART was evaluated. In addition, relative Doppler profile data were collected at the grid center covering the full range of potential DART operating points, and the effects of elevated background pressure and accelerator grid voltage changes were explored. The focus was on moly density and velocity profile variation across the grid face, including its dependence on parameters such as throttle point, and these results are complementary to quartz crystal microbalance deposition measurements. Combining LIF and QCM measurement data from the same location would allow direct conversion of LIF signal to absolute density, but this is difficult to achieve. An alternate approach was taken here, which also combines LIF and QCM data.

2. Materials and Methods

A tunable ring laser was pumped by a Millenia eV 15 Watt diode-pumped solid-state system, providing multi-line output at 532 nm. The unit is sealed and requires no laser head adjustments in normal operation. Although the pump laser does not operate with single frequency output, its amplitude stability and beam quality are good. The input power level selected for ring laser pumping was approximately 11 Watts. A Thermo Neslab RTE7 chiller provided temperature-controlled cooling water at low flow rate to the system, which is sensitive to temperature variations.

A Coherent 899-21 ring laser operated in Ti:Sa configuration generated tunable single frequency output that was locked to a scanning Fabry Perot reference cavity. A mix of short wave and medium wave optical elements installed in the ring cavity enabled usable power output over the 780–860 nm wavelength range without changing any optics. Typical power output at 855 nm was 0.8 Watt. The Ti:Sa crystal was temperature controlled either by a dedicated RTE7 chiller or by sharing a single unit that cooled Millenia diodes and Ti:Sa crystal in parallel.

A small portion of the ring laser output was split off to be monitored by a Burleigh WA-1500 wavemeter, with accuracy of about 0.002 wavenumber (specified accuracy of $+/-0.2$ ppm at the current wavelength) and a 1500 MHz optical spectrum analyzer. An optical telescope expanded the beam prior to admission to an MBD200 external frequency doubler. An LBO crystal optimized for 780 nm operation was used for frequency doubling. Output power at the 390 nm doubled wavelength, used for molybdenum LIF, was approximately 5 mW. Figure 1 shows an overall layout diagram for the laser system.

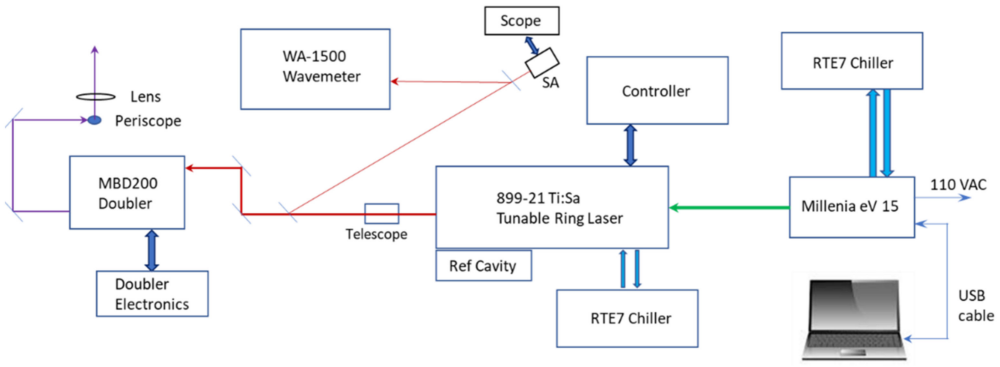

Figure 1. Diagram of tunable laser system used for the LIF measurements.

After converting the dye laser fundamental to doubled output, the resulting ultraviolet beam was chopped and sent up a periscope to a Brewster window port on the vacuum facility. The beam was sent through a collimator before passing through the thruster plume approximately 1 cm downstream of grid center, transverse to the thrust axis (see Figure 2). A photodiode near the far wall of the vacuum facility was used to verify the beam alignment or adjust as needed. At each LIF probe location across the 18-cm span from center to edge of the extraction zone, the laser beam remained tangent to the nearest point on the accelerator grid surface. The interrogation point was fixed in space, and the thruster was moved to permit measurements along a linear path from grid center to the perimeter on one side. To accomplish all this, the thruster had single-axis rotation (RS stage) and two-axis (X and Y stages) linear translation degrees of freedom. In Figure 3, the outer dashed circle and vector R_c defines the radius of curvature of the ion engine grids, X_0 is the distance between interrogation point and nearest grid surface, θ is the rotation angle from interrogation point to grid center, and R is the difference between R_c and the vector R_a, which extends from the RS stage axis of rotation to grid center. The positioning equations $RS = \theta$, $R = R_c - R_a$, $Y = Rsin\theta$, and $X = R(1 - cos\theta) + X_0$ were used. X and Y equal X_0 and 0, respectively, when $\theta = 0$. The grid angle displayed in data plots is referenced with respect to the grid radius of curvature. Axisymmetry was assumed for data analysis and interpretation to

remain within the scope of the study. Small deviations from axisymmetry are known to exist, based on more extensive current probe measurements [11]. Improved results could be obtained by collecting and analyzing data for a series of azimuthal angles.

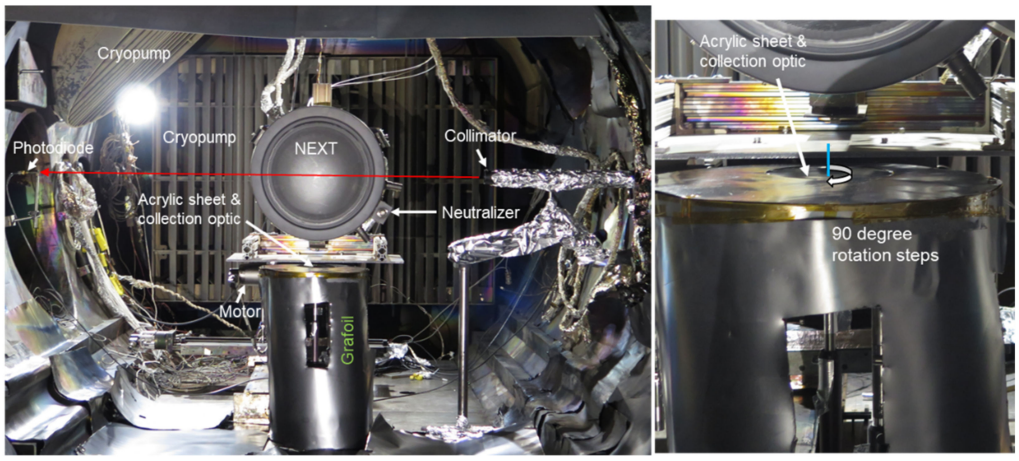

Figure 2. Photo of set-up inside the vacuum chamber (**left**), with magnified view of collection optic assembly (**right**).

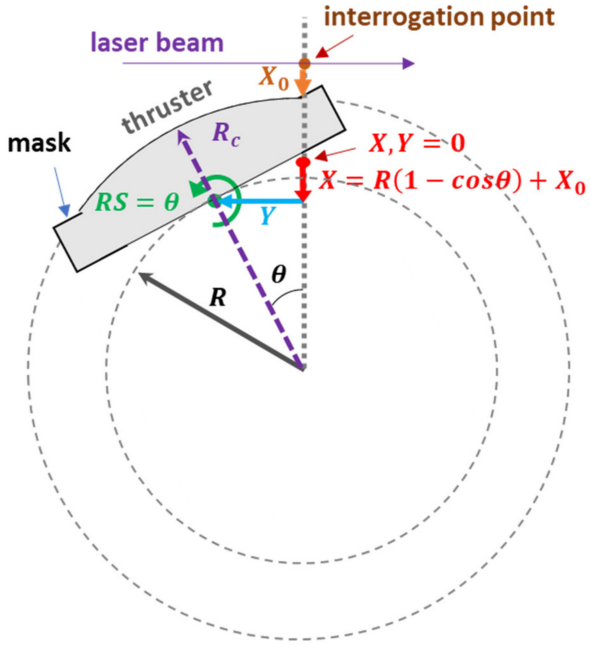

Figure 3. Diagram of thruster positioning relative to the fixed laser beam interrogation point, using rotation of the thruster and translation along X and Y axes to keep the laser tangent with a constant separation distance for each measurement location. R_a is not shown.

Quartz crystal microbalance (QCM) measurements were obtained separately on the same side of the grid, with a 15 MHz MK10 sun wise sensor made by QCM Research. This detector, its collimation system, typical scanning methodology, and other details have been documented previously [6].

Molybdenum atoms were excited from the ground state to an upper state that strongly fluoresces, using a transition at 390 nm. Resonance fluorescence was collected with a 15-cm diameter concave aluminum mirror, and the converging beam was guided vertically upward through a window port and focused into a 0.3-m McPherson 218 monochromator. The detector was a photomultiplier tube (PMT). The PMT output was fed into a lock-in

amplifier and demodulated via phase-sensitive detection at the chopping frequency. The laser frequency was scanned to record the Doppler profiles of sputtered molybdenum atoms at various grid locations. The relative density of molybdenum at each location could then be obtained by integrating over the Doppler profile. For one subset of LIF measurements at grid center, the laser frequency was parked at the peak of the Doppler profile. Laser scatter from the grid surface produced background signal that had to be subtracted from the molybdenum LIF signal. This was particularly an issue near the edge of the grid, due to scatter from the grid mask. At times X_0 was increased by as much as 1.3-cm to greatly reduce scatter from the mask. When this was done, a modest correction factor was applied to the molybdenum signal.

Because of moly sputter deposition around the engine, an acrylic sheet was mounted to a rotatable stage and positioned above the collection optic. The acrylic was transmissive at the fluorescence wavelength. The sheet was protected everywhere except above the mirror. By rotating the sheet in 90-degree steps under vacuum, an unexposed region could be placed above the mirror in case transmission of the previously exposed area was degraded. This could be done three times without overlapping a previously exposed surface. The collection optic was below the thruster, displaced approximately 7 cm downstream from the interrogation point to avoid occlusion of the collected fluorescence by the thruster.

NEXT was operated in the Aerospace EP2 facility, which is 9.8-m long and cylindrical with a 2.4-m diameter. Up to 10 PHPK cryopumps of re-entrant and standard 1.2-m designs can be operated simultaneously. The re-entrant pumps provide improved xenon pumping speed performance, up to 35,000 L/s each, with the drawbacks that the chamber internal volume is reduced and carbon backsputter rate is elevated. Data were obtained for various potential DART throttle conditions, with additional measurements on effects of elevating background xenon gas density and varying beam and accel voltage. To elevate background pressure, xenon gas was bled into the vacuum chamber through a sidewall port outlet about 1.8 m from the thruster, at a plume angle of approximately 45 degrees. The principal pressure gauge (Stabil-ion type ionization gauge) for background measurements was 1.3 m away, mounted off the chamber wall approximately 5 cm downstream from the grid apex. It did not have a line-of-sight view to the plasma inside the vacuum chamber.

NEXT has three distinct flow rates going through the neutralizer, the discharge cathode (DCA), and the discharge chamber. Direct flow into the discharge chamber (main flow) dominates the total and is the sum of the discharge cathode and the discharge chamber; this is what is plotted in Figure 4. For DART flight operations, the neutralizer flow rate is elevated substantially beyond the minimum needed. Flow rate variations were evaluated to $\pm$6% for the cathode (five settings) and the neutralizer (three settings), and to $\pm$3% for the main (three settings).

Throttle level TL28 is included in the standard NEXT throttle table; TT10 and TT11 are the latest versions [4]. In Figure 4, it corresponds to the flow condition designated as nominal ($\eta \approx 0.900$, discharge flow rate = 41.812); the flow variations are with respect to this throttle condition. The nomenclature DTLXX-Y-Z designates a DART throttle condition, complete with flow rates: D indicates the throttle level is DART-specific, Y indicates the total discharge chamber flow rate (sum of discharge cathode and main), and Z designates neutralizer flow rate; A is the highest flow rate and O is the lowest. The propellant mass utilization, η, is equal to $\dot{m}_I/\dot{m}_T$, where $\dot{m}_I$ is mass flow rate of ions from the thruster, and $\dot{m}_T$ is the sum of ion and neutral rates (total discharge chamber mass flow rate). The neutralizer exit is a significant distance downstream from the grids and to the side; its flow adds little xenon density at the grid face, and it is excluded from the total discharge chamber mass flow rate and most of the analysis we will describe. The neutral flow fraction is given by $1 - \eta$ and, for fixed beam current (I_b) conditions as normally employed in the present study, $(1 - \eta)/\eta$ is proportional to average xenon neutral density. To improve the accuracy of η figures used in the data plots, correction factors were estimated for both background gas ingestion by the thruster and Xe^{2+}/Xe^{+} fraction (about 4% in this case). The former correction assumed a Maxwell–Boltzmann velocity distribution and density

as measured by the wall ion gauge above the thruster. The latter correction was based on available NEXT measurement data for the Xe^{2+}/Xe^{+} fraction. Both corrections were small.

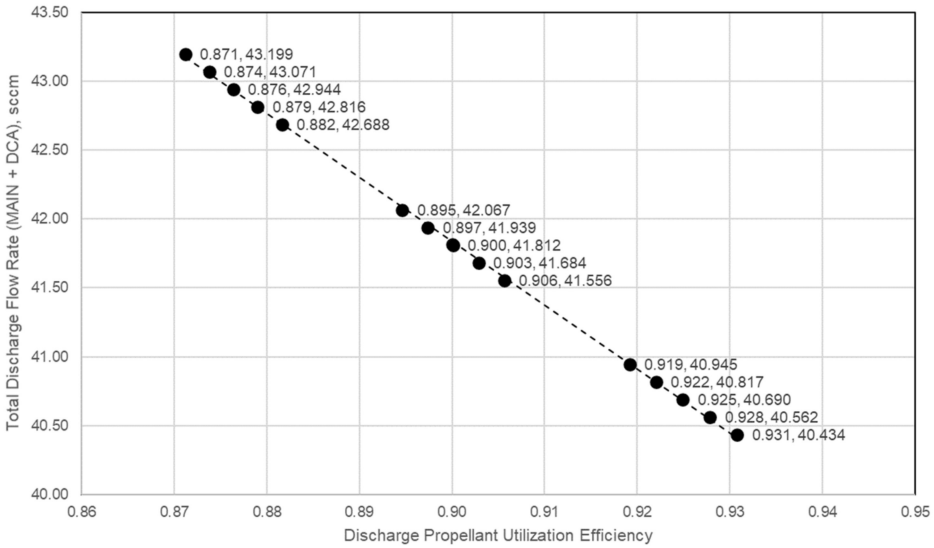

Figure 4. Flow rates and uncorrected mass utilization settings for evaluating NEXT over the range of potential DART operating conditions. The most "flooded" condition is at the upper left and corresponds to DTL28-A-A. The "nominal" condition is DTL28-H-H (0.900, 41.812), and most "lean" is DTL28-O-O (0.931, 40.434). Note that DTL28-H-H is equivalent to TL28 with respect to flow through the discharge chamber.

3. Results

3.1. Relative Erosion Rates at Grid Center

The dependence of LIF signal on the throttle condition was studied at grid center, with the laser frequency tuned to the center of the Doppler profile. For each setpoint, the beam current was 2.70 Amperes. Beam (V_b) and accelerator grid voltages ($-V_a$) are indicated in Figure 5, which plots the relative LIF signal amplitude at the peak of the Doppler profile, with additional engine parameters listed in Table 1. At grid center, this profile is highly symmetric, and its peak position coincides with the molybdenum rest frequency. To generate the plot, we have assumed the width of the Doppler profile to be constant, and the off-resonance signal due to laser scatter has been subtracted. The variation of molybdenum peak density indicates significant dependence on propellant mass utilization. This is to be expected if the erosion rate at the LIF probe location is strongly affected by ion–neutral charge exchange (CEX) interactions [5,12].

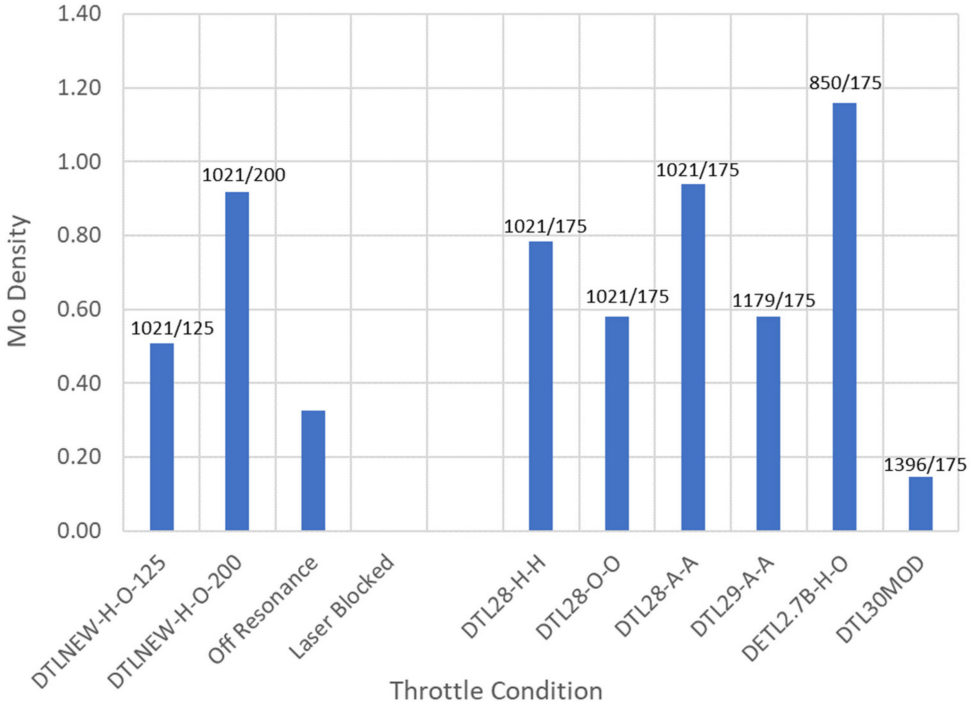

Figure 5. Relative peak molybdenum density at grid center as a function of throttle condition. Nominal ion beam (V_b) and absolute value accelerator grid voltages ($|V_a|$) are as shown, with throttle condition labels underneath. Table 1 provides additional information.

Table 1. Engine parameters for Figure 5 throttle conditions.

Throttle Condition	Ia (mA)	$(1-\eta)/\eta$	Facility Pressure (Torr; Corrected)	Flow Rates (sccm) Main/Cath/Neut
DTLNEW-H-O-1021-xxx	9.51	0.119	2.58×10^{-6}	37.54/4.26/4.71
DTL28-H-H	9.40	0.119	2.61×10^{-6}	37.54/4.26/5.00
DTL28-O-O	8.70	0.0788	2.50×10^{-6}	36.40/4.01/4.71
DTL28-A-A	10.0	0.155	2.73×10^{-6}	38.68/4.52/5.30
DTL29-A-A	9.90	0.155	2.76×10^{-6}	38.68/4.52/5.30
DETL2.7B-H-O	9.55	0.118	2.58×10^{-6}	37.54/4.26/4.71
DTL30MOD	8.85	0.118	2.67×10^{-6}	37.54/4.26/4.71

Ion–neutral CEX interactions convert fast ions into relatively slow ions, for which accel grid impingement probability is greatly enhanced. Their volumetric production rate is proportional to the product of neutral density and ion flux. Because total flow rate variation is small over the range of throttle conditions in Figure 5, neutral fraction in the source flow is clearly an influential factor. However, comparison of DETL2.7B-H-O and DTL30MOD, which have the same propellant utilization and accel voltage, reveals the critical importance of beam (or total) voltage. This is a general trend, apparent from the rapid falloff of moly density with total $(V_b + |V_a|)$ voltage, shown in Figure 6. The data were fitted to an exponential function, chosen on a phenomenological rather than theoretical basis. Most of the scatter in the plot is likely attributable to variations in V_a and η. A similar trend was observed previously, for data obtained over a range of the beam current, flow rate, and other variables [7]. For the present dataset, the beam current was not varied.

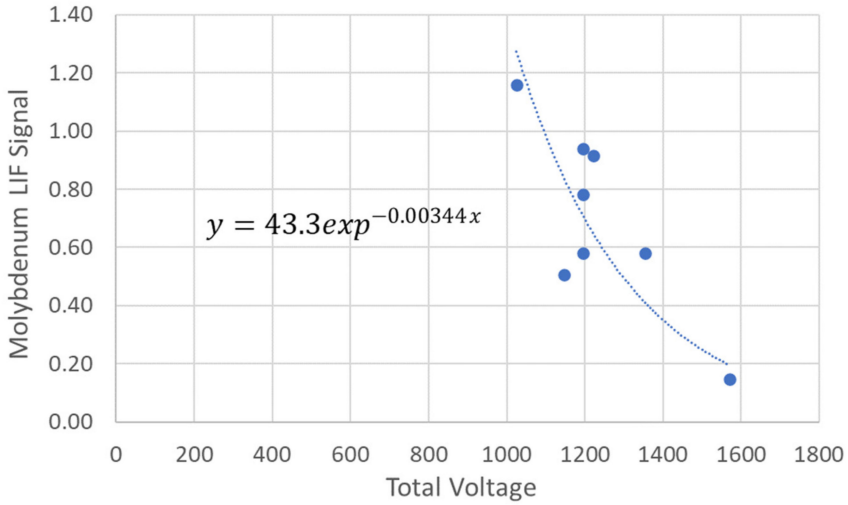

Figure 6. Relative peak density at grid center as a function of nominal total voltage for the throttle conditions included in Figure 5. The data were fit to an exponential function. Most of the plot scatter is due to variations in propellant mass utilization and accel voltage.

Comparison of moly density for the two "DTLNEW-H-O" cases indicates that accel voltage is also influential. A plot showing the "DTLNEW-H-O" cases with −125 and −200 accel voltages is given in Figure 7, together with DTL-H-H, which has the same discharge flow conditions. The Ia variation between these throttle conditions was several percent at most, with facility background pressure fluctuation determined to be the primary cause. Linear density dependence on $|V_a|$ is anticipated if most moly density results from ion accel impingement with energy driven by the magnitude of the accel voltage. The plot is consistent with that.

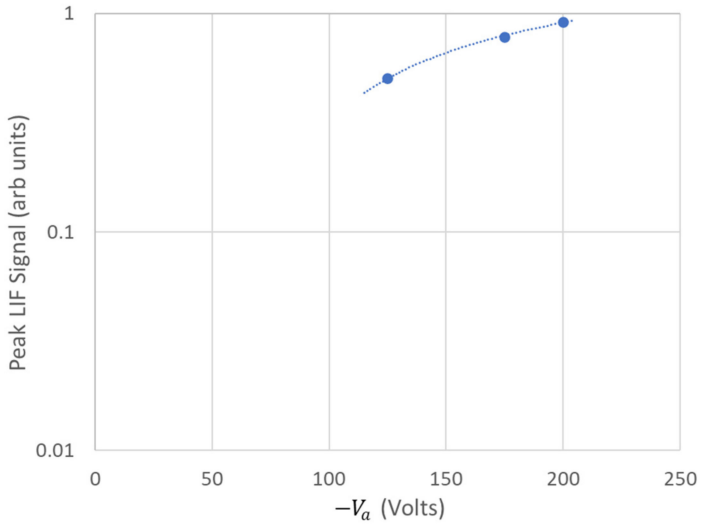

Figure 7. Effect of accelerator grid voltage on LIF signal at grid center for DTL28-H-H and DTLNEW throttle points (see Figure 5). Discharge chamber flow rates were identical.

In Figure 8, we present a collection of results. Among the findings are that average xenon neutral density (proportional to $(1 - \eta)/\eta$) extrapolates to zero long before Ia approaches it, background pressure similarly extrapolates to zero with nonzero Ia intercept, QCM signal extrapolates to zero concurrently with background pressure, and extrapolation to zero of moly density (LIF signal) at grid center correlates much better with $(1 - \eta)/\eta$ than with Ia. Figure 8d shows that the moly density at grid center is highly sensitive

to the relative change of Ia. In addition, LIF data were obtained while facility pumping speed was reduced due to fewer pumps operating, whereas two additional cryopumps were online during the subsequent QCM work. Ia changed proportionally to pumping speed despite equivalent background pressure. The source flow is identical, but with reduced pumping speed, lower bleed rate of background gas produced the same elevated background pressure. Because the background gas was fed in through a port that views the thruster, some of the gas collided directly with the accel grid and this may explain the slope change with pumping speed for the accel current vs. background pressure plot.

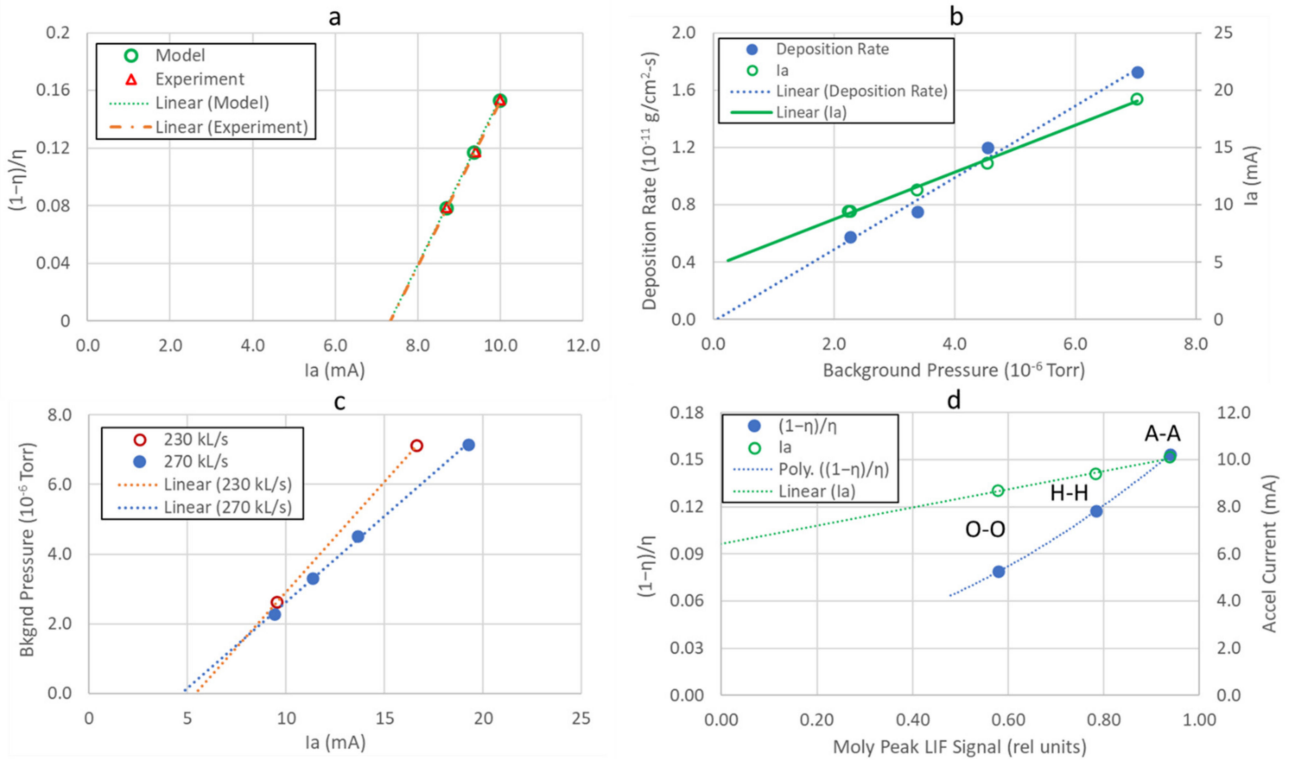

Figure 8. DTL28 parameter variations. (**a**) Dependence of accel current on the $(1-\eta)/\eta$ function; (**b**) QCM signal dependence on background pressure near peak of DTL28-H-H deposition rate profile; (**c**) accel current variation with background pressure; and (**d**) molybdenum peak LIF signal variation with accel current and $(1-\eta)/\eta$ at grid center.

3.2. Relative Doppler and Density Profiles across the Grid Face

Lineshape profiles at each of the five LIF probe angles across the grid face are shown in Figure 9. Profile shapes are due to the Doppler effect and were fit, in most cases, with a Gaussian function

$$f(x) = a_1 \exp\left(-\left(\frac{x-a_2}{a_4}\right)^2\right) + a_3, \quad (1)$$

where the a_i are fitting parameters. The largest angle, 17 degrees, was the only exception. Here the profile was clearly asymmetric, and the existence of a long tail on the high frequency side significantly reduced the quality of fit for the Gaussian function. For this case, a modified function with Thompson character [13,14] was utilized:

$$f(x) = a_1(a_2(x-12807.0))^2 / \left((a_2(x-a_5))^2 + a_3^2)^{a_4}\right) + a_6. \quad (2)$$

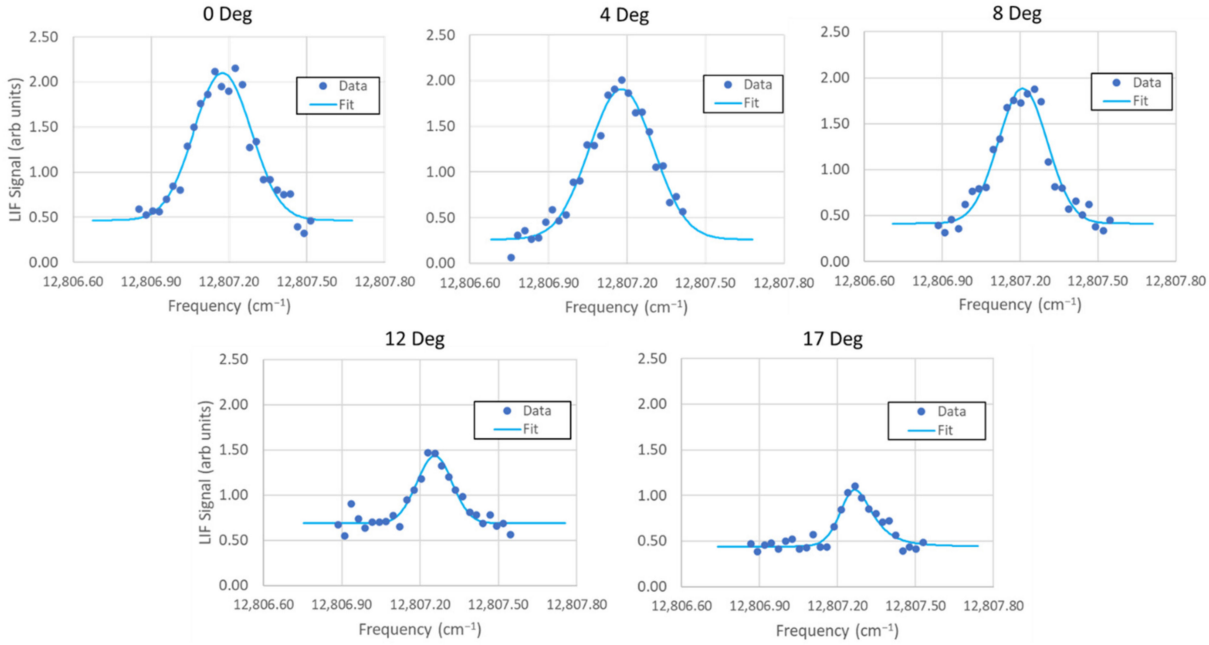

Figure 9. Molybdenum Doppler profiles at the five grid angles probed by LIF for DTL28-H-H. Progressive peak shifting occurs from grid center to edge, together with narrowing of the profile. Profiles are pure Gaussian at grid center and acquire significant Thompson character near the edge.

As shown by Figures 9 and 10, lineshape width was reduced by nearly half at high grid angles compared to its maximum. Laser frequency at the peak of the profile shifted progressively higher with angle, corresponding to a velocity component directed radially outward. The observed velocity profile was symmetric at grid center, whereas near the perimeter it was substantially asymmetric. Near the edge, the Doppler profile shows that most molybdenum atoms are moving radially away from the thrust axis, with few atoms traveling in the opposite direction.

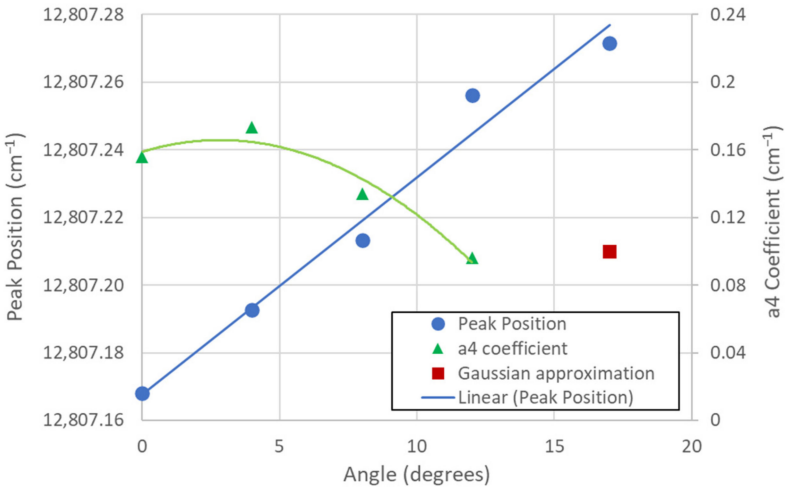

Figure 10. Measured position of peak Doppler profile for DTL28-H-H, from center to edge of grid. The a4 coefficient is a measure of width, obtained from fitting profiles with Equation (1).

The intensity of laser-induced fluorescence from sputtered molybdenum plume atoms, after integrating over the Doppler profile, is proportional to the particle density in the region of interrogation. Doppler profiles are Gaussian in nature for particles with a thermalized velocity distribution, and the averaged velocity vector is zero. Sputtered atom velocity

is more complex, with directed velocity away from the point of origin so that the sum of particle velocity vectors does not vanish. The Thompson distribution function works better to model such profiles if the laser beam is aligned with the most probable direction of motion from the sputter site. In the present case, the region of interaction between laser and interrogated molybdenum atoms is approximately 1 cm distance from the grid surface, and the laser beam passes tangent to the nearest grid point. Although the Doppler profile is really a hybrid with both Gaussian and Thompson character, we have been able to conveniently fit the measured Doppler profiles across the grid face using pure Gaussian functions, except for the 17-degree data points where the quality of fit is degraded. The width obtained from the Gaussian fit at 17 degrees is included in Figure 10 for comparison.

The Doppler shift of the peak profile density from grid center to edge was approximately 0.10 cm^{-1} at the fundamental laser frequency. The corresponding velocity shift was easily calculated, and we obtained 2.34 km/s, which is equivalent to 2.7 eV kinetic energy—about half the most probable energy for sputtered molybdenum atoms under low energy Xe^+ bombardment [15]. Accounting for the square root relationship between energy and velocity, we estimate the velocity component aligned with laser direction equals $V_0/\sqrt{2}$, and the most probable direction therefore crosses the laser beam at approximately 45 degrees. For low energy Xe^+-Mo sputtering with 45 degrees the most probable angle of efflux, the Xe^+ angle of incidence (AOI) is approximately 45 degrees off-normal and in the plane defined by surface normal and Xe^+ incoming trajectory [15]. The sum of these angles is roughly 90 degrees for the AOI range 30–70 degrees, although it increases slightly for higher AOI and decreases for lower AOI. Figure 11 depicts example impingement and efflux directions, with laser beam crossings that generate blue Doppler shifts consistent with results near the grid edge. We have CEX ion impacts on accel barrels by ions traveling in the downstream direction and similar impacts by ions traveling in the upstream direction, but the upstreaming ions will little affect molybdenum density in the region probed by LIF. Barrel impacts over a range of AOI values by downstreaming ions and accel downstream face impacts by upstreaming ions can both produce blue-shift laser crossings of the required magnitude.

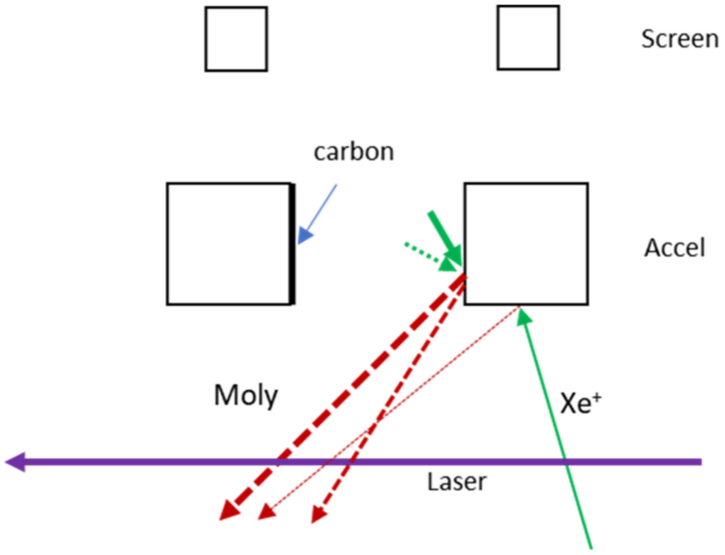

Figure 11. Diagram of a single screen and accel grid aperture pair (not to scale), illustrating hypothetical scenarios for Xe^+ impingement trajectories and associated directionality for peak molybdenum density distributions. The diagram applies to grid locations away from the center. Preferential carbon deposition sites and radial velocity of backstreaming CEX ions are potential causes of moly directional bias. Cusps are an artifact of the grid formation process and gradually wear away; they are not shown.

The grid fabrication process leaves a cusp in the middle of the accel barrel, which reduces its effective diameter and raises the barrel erosion rate. Residual cusps would have been present for the grid set used in the present study. Their existence changes the AOI distribution for both upstream and downstream ion barrel impingement and modifies the neutral densities. Upstreaming ions could produce significant Doppler shift at the laser crossing, even if well-aligned with the beamlet axis, due to cusp impingement. More details about cusp geometry are available in the literature [16].

Moly density decreases substantially across the grid face, especially near the perimeter, as shown by Figure 12, where the profiles were scaled according to the relative magnitudes measured at grid center (see Figure 5 results). The profiles depend on propellant utilization. With other factors remaining constant, moly density will vary with the local product of beam current density and neutral density. Beam current density has been measured near the grid face using a miniature planar probe, with less than 15% variation from 0 to 12-degree grid angle [11]. Whereas the source neutral density may change more than this, the anticipated moly density reduction at 12 degrees—even if background density made no contribution, although it certainly does—is less than observed. The reduced width of the Doppler profile at 12 degrees compared to 0 degrees and its peak shift are consistent with carbon deposition on the large-radius side of the barrel, or with radial velocity bias for CEX ion impingement on the downstream accel face at 12 degrees. Post-test grid inspection did suggest preferential carbon deposition on the large-radius side of barrels displaced from grid center, supporting the former explanation.

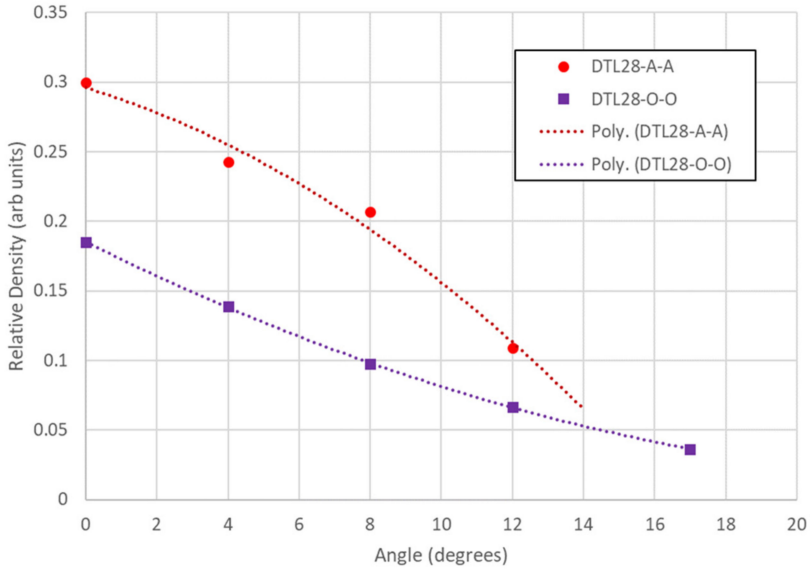

Figure 12. Relative molybdenum density profiles for high and low utilization DTL28.

The densities of source flow and background xenon neutrals will affect overall grid erosion rate as well as local rates, moly density profile across the grid, accel current collection, and so on. Rough estimates for source and background densities are given in Table 2. Accel grid current due to CEX ions created from background neutrals was estimated from the relation

$$I_a(bkgnd) = n_{bd}\sigma_{cex}l_d I_b, \quad (3)$$

where σ_{cex} is the CEX cross section for Xe^+-Xe [10], l_d is the effective distance over which charge exchange ions are collected, I_b is thruster beam current, and n_{bd} is the density of background xenon neutrals in the region where CEX ions are created and collected. This region can be considered to extend from a downstream surface outside the extraction grid system up to the plasma sheath near the screen grid. However, we ignore the intergrid region, as its contribution is relatively minor and stops at the downstream accel face. Each

of the parameters is well known except for l_d and possibly n_{bd}, which might be enhanced by a pileup of backstreaming neutrals at the downstream face of the accel [17–19]. A similar equation is written for source neutrals:

$$I_a(source) = (n_{su}l_u + n_{sd}l_d)\sigma_{cex}I_b, \quad (4)$$

where n_{su} is the intergrid (upstream) source density, and n_{sd} is source density just downstream from the accel grid. The contribution of intergrid Xe^+-Xe scattering to Ia has been neglected. For source flow, the accel current associated with downstream neutrals is expected to be larger than the upstream contribution, but not necessarily dominate the other. The l_d parameter is an unknown for source flow, as it is for background gas, and will vary with thruster operating parameters, such as beam and accel voltage [20]. Identical capture probabilities are assumed for downstream CEX ions, whether derived from source or background flow. The same 100% capture probability is assumed for intergrid ions, which can be a significant overestimate. Equating the ingoing transmitted flux for an accel aperture to the flux just downstream, we write

$$\frac{1}{4}n_{su}v_{su}K = n_{sd}v_{sd-ax}, \quad (5)$$

where v_{su} is the intergrid thermal velocity, v_{sd-ax} is the downstream average axial velocity, and K is the Clausen factor for the aperture. Estimating K as 0.6 and equating the two velocities based on Monte Carlo simulation results [21], we obtain $n_{su} \cong 7n_{sd}$. Assuming $l_d = 15l_u$, because the collection length for downstream ions is much longer, we rewrite Equation (4) as

$$I_a(source) = 1.5n_{sd}l_d\sigma_{cex}I_b. \quad (6)$$

Summing Equations (3) and (6) and allowing for an additional current source, we obtain

$$I_a(total) = (n_b + 1.5n_{sd})l_d\sigma_{cex}I_b + C. \quad (7)$$

Here, C accounts for current that remains when η = 100% and the facility has infinite pumping speed. Fixing the value of $1.5n_{sd}$ at 1×10^{11} cm^{-3} for DTL28-H-H (compare with density figures in Table 2), scaling n_{sd} according to $(1 - \eta)/\eta$, and applying Equation (7), the data plotted in Figure 8a can be modeled easily. For the model result shown, n_{bd} is 3.1×10^{11} cm^{-3}, l_d is 1.70 cm, and C is 1 mA. Increasing C to 2 mA drives n_{bd} down to 2.6×10^{11} cm^{-3}, with l_d equal to 1.68. Conversely, reducing C to zero pushes n_{bd} up to 3.6×10^{11} cm^{-3}, with l_d equal to 1.68. In all cases the $\frac{n_{bd}}{n_{sd}}$ ratio is substantially above the estimate of 1.4 obtained from a simple calculation of average densities (see Table 2). It is not unreasonable to expect the background density at the downstream grid face to be elevated above the ion gauge measurement at the wall. A portion of the neutral flux impinging on the accel downstream face may backflow from the beamstop with directional bias and elevated axial velocity [18,19]. Other complicating factors include the ~9% background pressure rise for the transition from DTL28-O-O to DTL28-A-A, which increases Ia and flattens the experimental data plot in Figure 8a. Correcting for this effect would reduce the rate of change of Ia with respect to η and further increase the background density when the data are modeled. Average collection length (l_d) and the effective enhancement factor for background xenon density relative to wall ionization gauge, both derived from the model, are listed in Table 3. The assumed value of C is especially influential on the enhancement factor, changing it by as much as ±25%.

Intergrid CEX ion impingement on accel barrels tends to be more efficient at producing molybdenum density at the LIF probe location than normal AOI impingement on the downstream face, because their potentially elevated impingement energy [22] and off-normal AOI [23] increases the sputter yield. The same is true for direct barrel impingement of beamlet ions, although we note that if AOI is very high—near grazing incidence—the sputter yield coefficient will drop accordingly. If the barrel impingement probability is

high, intergrid CEX ions may collectively contribute more to the probed moly density than downstream CEX ions.

Table 2. Rough estimates for average DTL28-H-H background and source densities.

Location	Background Density (cm^{-3})	Source Density (cm^{-3})	Total Density (cm^{-3})
Near Accel Grid, Downstream Side	9×10^{10} #	7×10^{10}	1.6×10^{11}
Discharge Chamber	$<9 \times 10^{10}$ #	2×10^{12}	2×10^{12}
Intergrid Region	$\leq 9 \times 10^{10}$ #	5×10^{11}	6×10^{11}

Density may be elevated due to high flux of backstreaming facility neutrals toward grids.

Moly sputter rate will be reduced wherever net carbon deposition is occurring. Central regions of the grid are little affected, but in outer regions beamlet current is reduced and net carbon deposition occurs, depending on throttle condition and specific location. If source density is also reduced, the effect of η on moly density becomes small, due to the small product of ion flux and neutral density and accumulation of carbon deposits. Figure 12 suggests that the effect of varying mass utilization tapers off at grid edge for the target DART operating point. Determining molybdenum efflux rate as a function of angle requires azimuthal integration at the polar angle of interest, so large-radius regions are weighted more heavily than central grid regions. Based on this observation, and flux enhancements due to off-normal moly directional preferences already discussed, we anticipate less utilization dependence for moly deposition flux recorded via quartz crystal microbalance (QCM) at 1 m than for near-field moly density at grid center. The data confirm this conjecture.

Table 3. Results of accel current collection model for DTL28. The collection length is also a measure of separation distance between ion beam neutralization front and accel downstream face.

Downstream CEX Average Collection Length, l_d (cm)	Background Density Enhancement Factor *
1.7	≈3

* Relative to wall ionization gauge measurement.

3.3. Absolute Density Model Based on Near-Field LIF and Far-Field QCM Data

As already discussed, integrated Doppler profiles are proportional to molybdenum density at each probed location. Each density obtained was treated as a quantity with arbitrary units. The relationship between relative and absolute density was expressed as

$$\rho_{abs} = k\rho_{LIF}, \quad (8)$$

where ρ_{abs} is the absolute sputter density, and ρ_{LIF} is the relative density obtained via LIF. The constant k is the conversion factor from relative to absolute units.

LIF data collected at 0°, 4°, 8°, 12°, and 17° from the thrust axis were fit to Gaussian curves. The five fitted curves were integrated and linearly interpolated, after subtracting baselines, to produce ρ_{LIF} as a multivariable function of angle and LIF frequency.

The scans of sputtered molybdenum LIF produce Doppler profiles corresponding to the velocity distribution component that is colinear with the laser beam. Molybdenum velocity components orthogonal to the laser beam do not produce a Doppler shift, therefore the two-dimensional velocity distribution is projected into one-dimension. Nonetheless, the 2D distribution can be reconstructed approximately by assuming it is rotationally symmetric about an axis through the peak of the observed LIF profile and azimuthally symmetric with respect to the grid. Off-center grid locations have non-zero directed velocity toward the periphery of the grid, enhancing their flux contributions at high angles with respect to the thrust axis.

The two-dimensional distribution was assumed to be Gaussian with the form

$$\rho_{rel}(V_x, V_y) = \frac{1}{2\pi\sigma^2} e^{-\frac{[(V_x-\mu_x)^2+(V_y-\mu_y)^2]}{2\sigma^2}} \tag{9}$$

where σ is standard deviation, a measure of profile width, V_x and V_y are two orthogonal velocity components in a plane with its normal defined by a ray pointing in the direction of maximum sputter density, and ray origin is at the grid location tangent to the laser beam. This plane is not necessarily tangent to the grid because the peak position of the LIF profile shifts to higher frequencies across the grid face, from apex to edge, indicating increasing radial velocity with distance from the apex. The shifted peak was assumed to only be shifted in one dimension along the axis of the laser beam. The variable V_y is the velocity component normal to the axis of the laser beam; V_x is in the same plane as the plane formed by the laser beam axis and grid normal. Because the plane of V_x and V_y may not be tangent to the grid, the component V_x may be angled with respect to the laser beam. This angle, ψ, is the same angle by which the peak axis is angled from the grid normal. The quantities μ_x and μ_y correspond to peak position with zero Doppler shift. Figures 13 and 14 illustrate the geometry involved.

The scans of sputter LIF describe Equation (9) integrated across the entire y-axis. Additionally, due to the shifted peak angles, the velocity component along the axis of the laser beam is equal to $V_x / \cos\psi$. Therefore, the relative density described by magnitude of the LIF signal is

$$\rho_{LIF}(V_x, \psi) = \frac{1}{2\pi\sigma^2} e^{-\frac{(V_x/\cos\psi-\mu_x)^2}{2\sigma^2}} \int_{-\infty}^{\infty} e^{-\frac{(V_y-\mu_y)^2}{2\sigma^2}} dV_y = \frac{1}{\sqrt{2\pi}\sigma} e^{-\frac{(V_x/\cos\psi-\mu_x)^2}{2\sigma^2}}. \tag{10}$$

Substituting the x-axis term in Equation (9) with Equation (10) gives the two-dimensional density distribution as a function of the measured relative densities and the y-axis term:

$$\rho_{rel}(V_x, V_y, \psi) = \frac{1}{2\pi\sigma^2} \left(\sqrt{2\pi}\sigma\rho_{LIF}(V_x, \psi)\right) e^{-\frac{(V_y-\mu_y)^2}{2\sigma^2}} \tag{11}$$

Because the distribution is assumed to be axisymmetric, the function can be evaluated at the y-value that corresponds with the peak position of the two-dimensional distribution, i.e., the origin of the distribution, where $V_y = \mu_y$. The relative density can be evaluated as a function of only V_x and the shifted peak angle:

$$\rho_{rel}(V_x, \psi) = \frac{\rho_{LIF}(V_x, \psi)}{\sqrt{2\pi}\sigma}. \tag{12}$$

The standard deviation was found from fitted curves for the interpolated LIF data. Equation (12) shows that the flattened two-dimensional Gaussian simply scales the true distribution by a constant. Because the data are relative with only arbitrary units, the constant multiple in Equation (8) can be neglected when correlating the far field flux prediction and the QCM data, but the value of the conversion factor is important when determining absolute densities across the grid face, and so the additional terms in Equation (12) are included for all calculations.

To find the conversion factor to translate the relative mass units to absolute units, the LIF relative density data were correlated with mass flux QCM data. The QCM measurements were taken at a 1 m distance from the grid. Therefore, in order to correlate the relative LIF data with the absolute QCM data, the LIF data were used to predict the mass flux of sputter at the distances corresponding to the QCM measurements. This prediction provides insight into the mass flux across the entire 1 m far field, and it produces the conversion factor to compute absolute densities for sputter across the grid face. The prediction was calculated in MATLAB by approximating the geometry of the thruster grid, grid mask, and 1 m far field. The discrete elements of the geometries were then used to ray-trace

sputter trajectories from the grid face to the far field. Performing these calculations over the grid face area and summing their contributions at each far-field location produced a prediction for relative sputter mass fluxes at 1-m distance in the horizontal plane. This result could then be correlated with QCM data to produce the desired relative-to-absolute conversion factor.

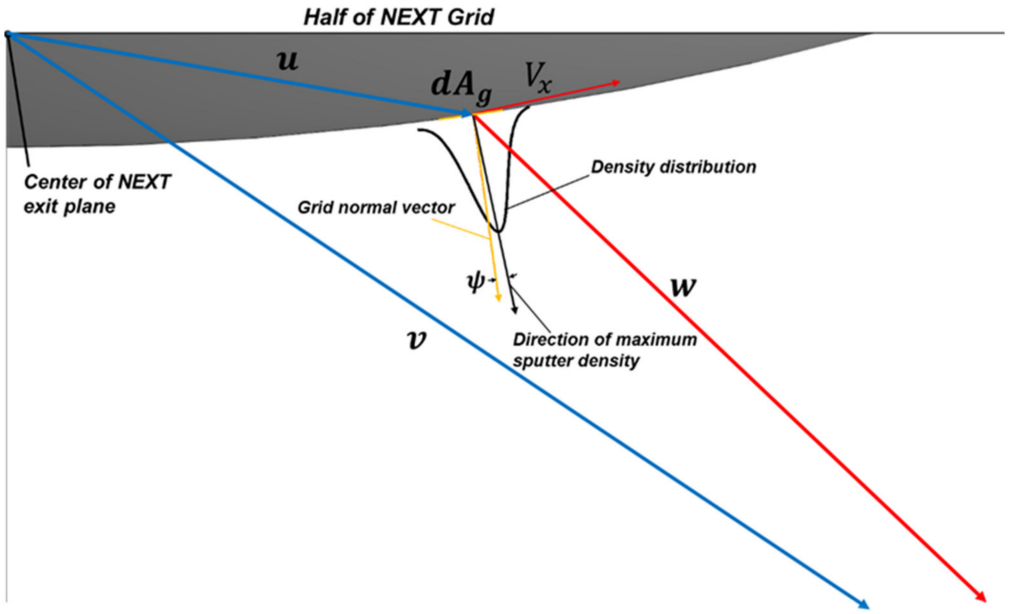

Figure 13. Diagram of one-half of the NEXT grid, and shift of average velocity vector for moly sputter efflux with respect to local grid normal.

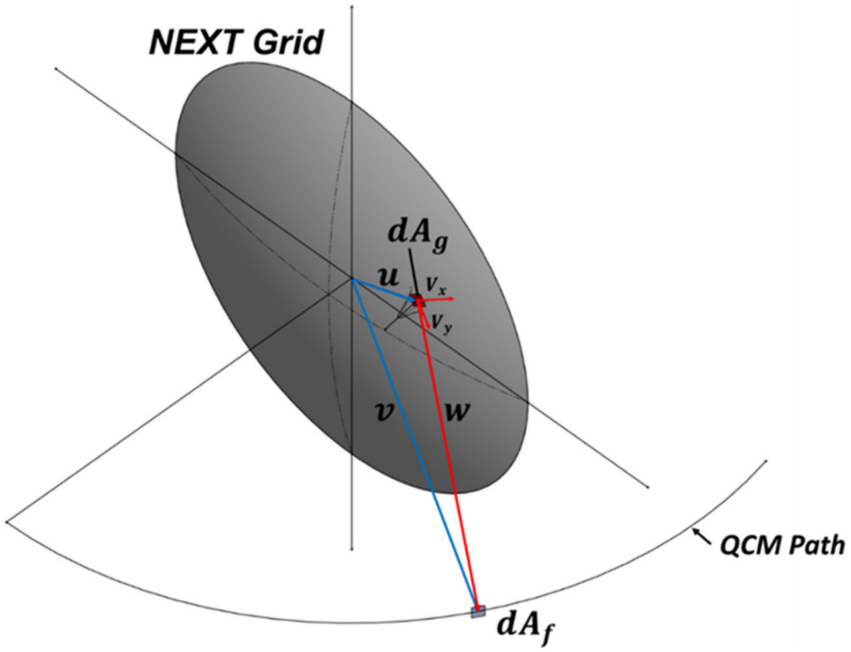

Figure 14. Diagram showing an arbitrary area element near the NEXT grid face and coordinate system for analyzing its contribution at an arbitrary location along an arc 1 m from thruster.

The grid and grid mask were discretized into matrices of points in vector space, where the coordinate system origin was set at the center of grid curvature. The grid geometry was assumed to be a spherical cap with defined radius of curvature. The LIF relative density

measurements were assumed to occur at this radius, even though in the experimental setup the measurements were taken at points approximately 1 cm distance from the grid face. The range of polar angles that describes the grid active area was assumed to be $+/-15^{\circ}$. The grid was discretized into elements with size 1° polar and 1° azimuthal, relative to the stated coordinate system. The grid and grid mask were discretized into matrices of points in vector space, where the coordinate system origin was set at the center of grid curvature.

The grid mask was assumed to be conical in shape, where the edge of the cone approximates the furthest edge of the grid mask, and the cone apex is at the origin. This assumption was made because any particle with trajectory above this grid mask edge is unaffected, whereas any particle below is obstructed by the grid. This is identically accomplished with the conical geometry. The cone was discretized into elements with size 1 cm radially by 10° azimuthally. The grid mask element coordinates were then triangulated to produce a triangle mesh.

The far field was approximated as an arc along a spherical surface with radius equal to 1 m and origin at the center of the grid exit plane. The arc corresponds to a path along the spherical surface at azimuthal angle 0°. The points in the far field were parameterized as a function of their angle from the thruster exit plane. Again, the origin of each point was set at the center of curvature of the grid. The plane of the QCM was assumed to be normal to the line drawn from the center of the grid exit plane to the given point in the far field.

The flux of moly sputter in the far field was predicted from the LIF grid sputter densities by summing the differential flux from each differential grid area for any given point in the far field. The differential flux for any given differential grid area was determined by first finding the sputter flux at the grid and then calculating the mass flow from the grid element to the far field. The sputter flux at the grid was found from the product of the local sputter density and speed,

$$dj_g = \rho_{rel} V. \tag{13}$$

The local sputter density, ρ_{rel}, was found from Equation (12), where the density is a function of V_x and the peak shift angle, ψ. Both are functions of the given differential grid area, dA_g, and the polar angle of the given point in the far field, θ_{f_o}; dj_g is the differential flux at the grid. The sputter speed, V, is assumed constant.

The velocity distribution of sputtered particles was assumed to be independent of angle—both polar and azimuthal with respect to the grid aperture normal. The constant speed value was found by averaging the speeds of sputter with incidence angle 30° and field angle -45°, weighted by the relative sputter densities [15]. The constant speed used was 0.497729 cm^{-1} or 5.83×10^5 cm/s, assuming an unshifted wavenumber of 25,614.357 cm^{-1}.

The local sputter density, ρ_{rel}, is a function of the given grid differential area position and the given point in the far field. The position vectors of each are used to find the sputter density from Equation (12) and the interpolated LIF data.

The vector that describes the path of a sputtered moly particle is $\boldsymbol{w}$, and it can be found for any given point in the far field and any given differential area on the grid by subtracting the position vector of the grid differential area, $\boldsymbol{u}$, from the position vector of the far field point, $\boldsymbol{v}$. Put concisely:

$$\boldsymbol{w} = \boldsymbol{v} - \boldsymbol{u}. \tag{14}$$

With the assumption of constant speed sputter particles, the sputter velocity is given by

$$\boldsymbol{V} = \boldsymbol{V}\hat{\boldsymbol{w}}, \tag{15}$$

where $\hat{\boldsymbol{w}}$ is the unit sputter vector, normalized from Equation (14). The density of moly sputter in the direction of $\hat{\boldsymbol{w}}$ was found by inputting the velocity $\boldsymbol{V}$ into the relative density function derived from the interpolated LIF data. This was done by taking the sine of the angle between $\boldsymbol{w}$ and the density distribution's axis of symmetry. The result is the Doppler-shifting velocity component, which, converted to wavenumbers, can be inputted

into Equation (12), where the LIF relative density function is the multivariable function from the interpolated LIF data. With the sputter speed and relative density at the grid in the direction of the given point in the far field, the differential flux can be found from Equation (13).

The net mass flow from the grid differential area, dA_g, to the far field differential area, dA_f, is described by

$$dj_g dA_g d\Omega_f = dj_g dA_g \frac{dA_f \cos\theta_f}{R^2} \tag{16}$$

where $d\Omega_f$ is the solid angle with which dA_f is seen from dA_g; R is the distance from dA_g to dA_f, and θ_f is the far field angle between the far field normal and the incident sputter vector. The mass flux in the far field was desired, and so dA_f was divided out of Equation (16). Therefore, the far field flux is

$$dj_f = dj_g dA_g \cos\theta_f R^{-2}. \tag{17}$$

Combining Equations (12), (13), and (17) gives a final function for the far field mass flux using the described geometry and measured data,

$$dj_f = \left(\frac{\rho_{LIF}\left(\theta_{dA_g},\, \theta_p\right)}{\sqrt{2\pi}\sigma} V \right) dA_g \cos\theta_f R^{-2}. \tag{18}$$

The total sputter flux at a given point in the far field from the grid is given by the summation

$$j_f = \sum_{i=1}^{N} \left(\frac{\rho_{LIF}\left(\theta_{dA_{gi}},\, \theta_{p_i}\right)}{\sqrt{2\pi}\sigma} V \right) dA_{g_i} \cos\theta_{f_i} R_i^{-2}, \tag{19}$$

where N is the number of discrete grid elements.

Not all grid elements contribute sputter flux to a point in the far field—there are two factors preventing a given element's contribution: occlusion by the grid and occlusion by the grid mask. To calculate occlusion by the grid, all elements were neglected whose sputter vector had an obtuse included angle between it and the given element normal vector. Because the grid geometry is spherical, any sputter vector with an obtuse angle intersects the grid itself, and so the given element cannot contribute flux to the far field.

Grid mask occlusion was calculated by finding the intersection point between the sputter vector and every plane of the mask triangulation. If the intersection point was within the triangle that defined the plane, then the sputter vector was obstructed, and any contributions from that grid element were neglected.

Using these methods, the flux of moly sputter for a given point in the far field was calculated. Iterating this calculation over the entire far field produced the complete flux prediction. The calculation was performed for angles -13° to 90° from the thruster exit plane.

With the complete prediction, the QCM data and far field prediction were correlated by assuming they were related by a single constant, as described by Equation (8). The conversion constant was found by correlating the two datasets at angles from the grid exit plane of 12° and 16° and averaging the conversion factor for each. This conversion factor was then applied to both the far-field flux prediction and the grid density plots. Figure 15 shows the 1-m distance predicted absolute flux profile based on the near-field LIF measurements calibrated with a selected portion of the raw QCM data, also plotted. The shape of the predicted moly flux profile deviates strongly from a simple cosine approximation due to the variation of production efficiency across the grid and preferred directionality.

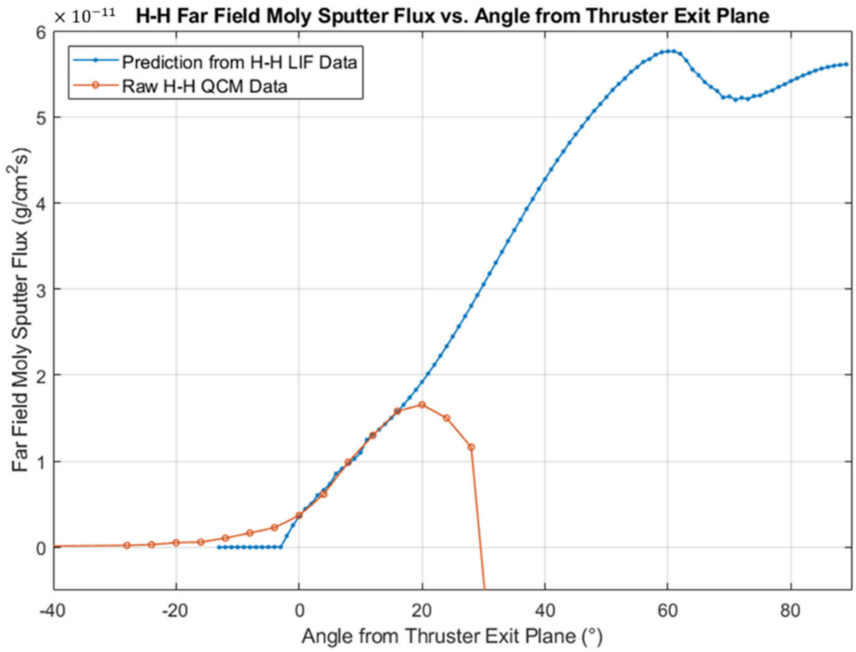

Figure 15. Sputter flux profile along 1-m arc for DTL28-H-H operating condition, based on near-field LIF measurement correlated with QCM data for absolute flux determination.

At larger forward angles, ion flux wins out over moly deposition, and the QCM records net erosion. In the backflow region, the grid mask eliminates line of sight from the grid, but the QCM still detects low level deposition. The signal may be due to moly ions whose trajectory is bent by local plume electric fields into the backflow region [24]. Figure 16 plots absolute moly sputter densities near the grid face. A simple linear fit was performed, without theoretical justification.

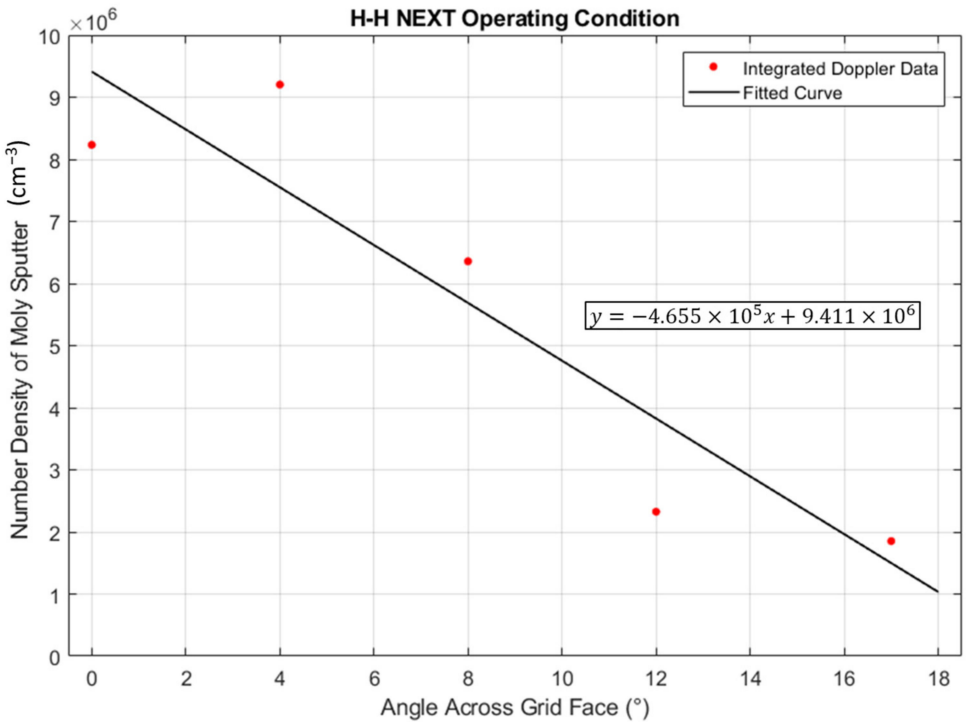

Figure 16. Absolute molybdenum density near the grid face for DTL28-H-H.

Although the QCM data provide absolute deposition rate figures, the angular profiles generated typically involve significant uncertainty. This is because of several factors, including the complexities of slow deposition in a vacuum environment with low levels of residual gases and sensitivity to the local thermal environment because of imperfect sense and reference crystal matching.

4. Discussion

An ion optics set built to the DART standard was unavailable until after these LIF and QCM measurements were performed in late 2017–early 2018, therefore an engineering model grid set was utilized. This grid set had been operated for several hundreds of hours at the time, compared to several thousand for our previous LIF and QCM work [6,7]. The peak deposition rate of the newer grid set was similar, according to QCM results, but their behaviors differed in some other respects. Although NEXT design reduces the effect, barrel wear is still significantly elevated early in grid life [25].

Background neutrals approaching the screen grid from downstream have the advantage of not crossing a region with an intense, ionizing flux of electrons. Therefore, instead of becoming ionized and driven away by the electric field, most passing through an accel aperture will reach the screen grid. If the flux of these neutrals into the grid set is enhanced, as the analysis indicated, and directional, the strong influence of elevated background pressure on erosion rate that is typically observed becomes more understandable. In previous QCM work and for DTL28-H-H in the present study, it was found that the observed deposition rate was approximately proportional to background pressure for most operating points [6]. TL12 was a very notable exception. TL12 has over-focused beamlets at grid edge, resulting in onset of direct impingement there. Elevated background density was found to *reduce* the deposition rate rather than increasing it. Evidently, the elevated density flattened the curvature of the plasma sheath at the screen grid, moving ion trajectories away from the over-focused condition and thereby reducing direct impingement and erosion rate at the grid edge [6]. In contrast, this effect on trajectories will *increase* barrel impingement if beamlets are already under-focused, a condition associated with much higher ion throughput than pertains to TL12. Therefore, other operating points—for example DTL28-A-A—may receive a boost in barrel erosion rate from this effect in addition to the higher CEX production during the transition from DTL28-H-H.

Based on past experimental and theoretical work, it is expected that all CEX ions formed in the region between accel grid and the downstream point at which ion beam neutralization is reached will be drawn upstream and impinge on the accel grid [25–27]. This distance is the neutralization length, which we equate to l_d. Impingement occurs on the downstream face and barrel and possibly the upstream face. Variation of beamlet current and beam voltage is predicted by simulations to moderately affect the value of l_d [20]. Theoretical treatments struggled to produce realistic neutralization length estimates, finding values that were too small [26]—much less than 1 cm. Later work was generally consistent with $l_d \approx 2$ cm [25,27], which is close to our estimated value (see Table 3). The distance is nominally determined by the position where beamlets have merged to produce plasma of approximately uniform potential. This location will vary with beamlet current, beam and accel voltages, propellant utilization, background neutral density, and grid geometry; all these parameters influence ion trajectories. Some fraction of CEX ions formed further downstream of the neutralization point may also contribute to accel current.

Extrapolation of DTL28 flow settings to 100% propellant mass utilization (zero neutral density from source flow) coincided with about 7 mA residual accel current (Ia). Extrapolation from DTL28 to zero background density coincided with about 5 mA residual Ia. In each case, a linear relationship was found. The accel current contribution was higher for background neutrals compared to source neutrals, on average. Grid-center moly density varied quickly with Ia and more slowly with source neutral density (see slopes in Figure 8d). It extrapolated approximately to zero as η approached unity, whereas LIF signal was completely lost with much more modest Ia percentage change. Here it is important to

remember that moly relative density was a local measurement, whereas Ia and $(1-\eta)/\eta$ are "global" parameters averaged over the entire grid area. Beamlet current is higher near grid center compared to grid edge, and the same may be true for source density, yet the periphery is weighted more strongly due to area factor. NEXT was designed for improved beam flatness [28], but the variation that exists still limits the beam extraction capability. The neutral density profile is unknown, and although the design was intended to avoid the severe neutral depletion observed with NSTAR [29], the dual peaks in the Xe^{2+} beam profile [11] suggest a double dip neutral profile. Background gas density, in contrast, is nearly constant over the grid face, so dependence of moly density on source flow compared to background gas is enhanced at grid center.

The rapid variation of grid-center moly density with Ia is consistent with greater Ia change at grid center compared to grid average. A similar statement applies for source flow xenon neutral density as reflected by $(1-\eta)/\eta$, although the contribution of background gas reduces the percentage change for overall xenon neutral density as η is varied. In any case, if 7 mA of accel current remains after excluding the source density, and 5 mA of that is related to background gas, additional factors may contribute on the order of 2 mA (see Table 4). One of these potential sources is the ion beam neutralizer [30], another is direct impingement by primary beamlet ions.

Table 4. Rough estimate of accelerator grid current contributions for DTL28-H-H.

Contributor	Downstream Face (mA)	Barrels (mA)	Energy (eV)
Background gas neutrals	5 *		≤175
Downstream source gas neutrals	1.5 *		≤175
Intergrid source gas neutrals		0.7	varies
Neutralizer, direct impingement		≤2	low-high

* Some impingement may occur on the accel barrels and upstream face, and therefore not contribute to density in the LIF probe region.

Dependence of QCM deposition rate on background pressure, as plotted in Figure 8b, indicates that background pressure is the dominant factor producing high angle moly flux in the far field. The inherent QCM view factor to various grid elements and radial bias of moly flux from those elements enhances the deposition rate profile at high angles from the thrust axis. Plots in Figure 12 suggest that the relative importance of source to background neutral density decreases from grid center to edge, helping to ensure the deposition rate registered by the QCM is dominated by background gas. A similar pressure dependence study was not performed for LIF signal across the grid, but two-point measurements at both grid center and edge found DTL28-H-H moly density increased quickly with background pressure. However, here the situation is clearly complicated with multiple factors contributing to the observed erosion. Figure 7 data show that molybdenum density is strongly influenced by accel collection of CEX ions with kinetic energy that tracks V_a magnitude.

Moly density change from DTL30MOD to DTL28-H-H throttle condition was particularly dramatic, as documented in Figure 6. The only difference is V_b = 1021 V for the latter condition and 1396 V for the former; background pressure and utilization nominally did not change. The value of Ia increased from 8.85 to 9.4 mA during the transition to lower voltage. For comparison, Ia increased from 8.7 to 9.4 mA for the transition DTL28-O-O to DTL28-H-H, with 35% moly density enhancement, and the density ratio for the DTL30MOD to DTL28-H-H transition was 5.3. These numbers appear to require that ions associated with the accel current increase for DTL30MOD to DTL28-H-H produce probe region moly much more efficiently than those associated with the DTL28-O-O to DTL28-H-H increase. The efficiency ratio could be estimated as $(0.7\text{ mA}/0.55\text{ mA})(430\%/35\%) = 15.6$, except that we expect the accel current increase when beam voltage is lowered to go preferentially to grid center and other regions with high beamlet current. Utilization, like beamlet current, is not uniform over the grid area, and source neutral density across the grid face is unknown, as it has not been measured during thruster operation. It is reasonable to assume the

source neutral density at any given location is proportional to $1 - \eta$ if the beam current is fixed. If the current increase for the DTL30MOD transition occurs over just 25% of the grid area (uniformly), whereas the increase is over the entire grid for the DTL28-O-O case (and uniform), the efficiency ratio is about 4—a more feasible ratio to explain but still challenging. Even more challenging to rationalize is the observed 430% increase of moly density for a fractional accel current increase of just 6%.

Providing further evidence for different efficiencies in producing detectable moly efflux at grid center is the very high DETL2.7B-H-O erosion rate shown in Figure 6. DETL2.7B-H-O has higher mass utilization than DTL28-A-A, yet moly density is also higher. It matches the DTL30MOD utilization, yet moly density is about 8× higher for DETL2.7B-H-O (V_b = 850, V_a = −175) compared to DTL30MOD (V_b = 1396, V_a = −175). We attempt to explain this result as follows. Ion trajectories expand radially outward in the intergrid region as the beam voltage is lowered, reducing the axial to radial acceleration ratio and making barrel impingement more probable for a subset of CEX, primary, and scattered ion trajectories. As total voltage decreases and impingement rate rises, the average impingement energy is also increasing, and the average AOI for these ions is near the peak of the angular sputter profile (the sputter yield is about twice as high for 45 to 60-degree AOI compared to normal or near-normal incidence)—leading to much higher sputter yield and moly density production in the LIF probe region. Sputter yield gain up to 15× can result from impingement at the full total voltage (~6×) rather than $|V_a|$, together with more favorable AOI (≤2.5×) [31]. The intergrid accel current is estimated to be about an order of magnitude lower than the sum of downstream background and source current (see Table 4), but this statement applies globally for the accel surface and not necessarily at grid center. Based on Figures 8d and 12, propellant utilization dominates the moly signal at grid center for DTL28, although not at the edge. At the center, beamlet current approaches the perveance limit, increasing the collection of upstream ions on the barrels. If neutral density is raised via reduced propellant utilization or elevated background pressure, CEX ion production increases, but the plasma sheath becomes even flatter to further elevate upstream ion collection. However, raising the beam voltage increases sheath curvature and causes ion trajectories to be focused more strongly. This greatly reduces barrel collection of upstream ions and reduces the neutralization length as well, as the beamlet diverges more rapidly after passing through the accel aperture. Collection of CEX ions formed from downstream source neutrals and background neutrals decreases, especially at grid center where the collection distance is well below the global average. Average impingement energy decreases as well, as the average location and its potential where downstream ions are birthed is closer to the accel. The high current beamlets constitute just a fraction of the total number, and as downstream collection current drops with increased beam voltage at grid center, Ia is less affected. Considering all these factors together, the 8× erosion rate reduction for DTL30MOD relative to DETL2.7B-H-O seems understandable.

The measured behavior of NEXT with nominal and reduced grid gaps indicated constant Ia over a wide total voltage range for the reduced gap but steadily declining Ia with increasing voltage over a similar range for the nominal gap [32]. DETL2.7B-H-O is close to the perveance limit, defined as the beam or total voltage for which $\Delta Ia/\Delta V = -0.02$ mA/V. This occurs around the knee of the Ia vs. V_b plot, and the limit is always preceded by nonzero slope over a significant range of voltage due to beam ion direct impingement. Both primary beamlet ions and high energy CEX and scattered ions can contribute to the barrel erosion, and behavioral similarities with respect to change of beam voltage are expected. We conclude that ion impingement at energies much higher than characteristic of accel voltage contributes to the LIF signal over at least a portion of the grid area and can be greatly reduced by raising the beam voltage.

Theoretical simulations provide significant support for the hypothesis we have outlined. In one instance, similar average erosion rates were found for accel barrel and downstream face, early in grid life [20]. In a second study [16] (see Figures 10 and 11), CEX ions for each termination surface—barrel, downstream, and upstream faces, etc.—are

shown according to their region of formation for several total voltages. Here it is apparent that the lowest beam current case has much greater barrel impingement by high energy CEX ions.

Possible explanations for the radial velocity bias of sputtered atoms include preferential carbon deposition masking of accel grid erosion on one side of the beamlet aperture, beamlet asymmetry, and off-normal impingement bias of backstreaming CEX ions on the downstream accel face. Inspection of the apertures revealed substantial, progressively asymmetric wear from grid center to edge, and significant carbon deposition. High backflux of carbon atoms is a feature of the test facility, due to internal cryopump surfaces that see direct ion impingement. Back-sputter rate estimated via a witness sample measurement was approximately 2.3 μm/kh for DTL28-H-H. Carbon masking on one side of the barrels, due to differing downstream view factors, potentially leads to a peak shift for the Doppler profile, growing progressively with radial distance as carbon deposition increases. This was illustrated by Figure 11, but quantification of carbon deposition was not performed, and its distribution is likely complex. The peak position moves mainly by elimination of a portion of the Doppler profile, rather than an overall shift. Evidence is mostly lacking that ions impinge on the downstream accel face with the necessary radial direction bias, although we do observe radial bias at the grid edge, as illustrated by Figure 17. However, this does not appear to be consistent with regular progression of the Doppler profile peak position. Instead, it is a phenomenon associated with the final few apertures at the edge, presumably due to beamlet space charge, which becomes radially unbalanced near the perimeter. The erosion pattern superimposed on areas of net carbon deposition suggests that downstream CEX ions acquire radial velocity of the same order of magnitude as axial and therefore impinge radially outward from apertures along the perimeter. Their motion does not always follow a straight line, as indicated by arrows in Figure 17, because the hole pattern is not azimuthally symmetric. The long tail observed in the Doppler profile at grid edge, which degrades the quality of Gaussian fits, likely results from this radial bias and strongly off-normal AOI of the charge exchange ions. The aperture (barrel) wear trend is progressively more asymmetric with the radial coordinate, which may be driven by radial potential gradient, aperture misalignment, nonuniform carbon deposition in the barrel, or other factors. Carbon deposition may exert the most influence.

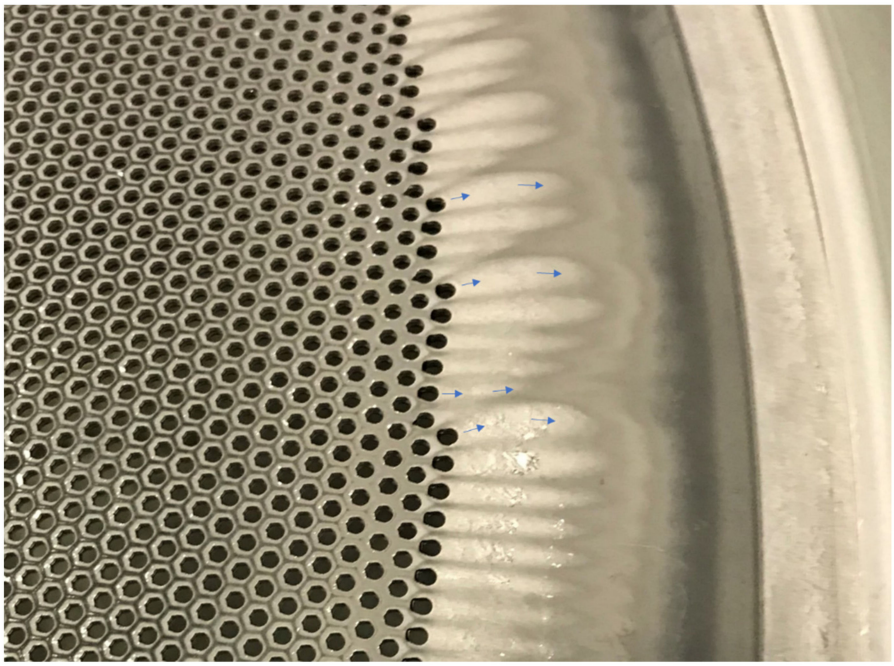

Figure 17. Photo of grid periphery showing the erosion-deposition pattern. Net erosion emanates radially from the peripheral set of holes, with directionality influenced by the hole pattern.

Other factors to consider in relation to radial velocity bias of sputtered molybdenum are alignment offset between screen and accel apertures, electric-field driven radial velocity bias of discharge chamber ions as they encounter the screen grid plasma sheath, and ion density gradients behind screen apertures. The effect of each of these factors has been simulated, and experimental data showed that they produce an offset of the pit and groove erosion pattern on the accel downstream face [33]. The offset is in the direction of the beamlet steering. An offset toward the small-radius side of the aperture is apparent in Figure 17, which is inconsistent with expected radial velocity bias (whether it is due to electric field or plasma density gradient) for discharge ions near the perimeter. Grid alignment offset combined with carbon deposition that correlates with the radial coordinate may therefore be the primary cause of biased molybdenum radial velocity. If correct, we would expect to measure something different on the opposite side of the grid. For the present study measurements were performed on one side only.

5. Conclusions

The present study is the first to systematically vary flow conditions and other parameters while measuring real-time ion engine erosion rate across the grid face, with analysis of these results in the context of the overall erosion process. Erosion rate was found to be well behaved over the NEXT throttling envelope for DART, with no significant lifetime concerns.

Results indicated pronounced rolloff of erosion rate from grid center to edge and strong variability at grid center. Four main sources of grid erosion were elucidated for DART operating points: (a) downstream CEX from background; (b) downstream CEX from source flow; (c) intergrid CEX from source flow; and (d) direct impingement. Additional contributors are ion–neutral intergrid scattering and ions from the neutralizer cathode. Evidence was found for elevated energy charge exchange ion impingement and beam ion direct impingement on accelerator barrels in the central grid region at low beam voltage. This increases as beam voltage is lowered at a fixed beam current and can dominate the local erosion process if the beamlet current is near the perveance limit. Raising the beam voltage modifies the intergrid ion trajectories and can substantially reduce beam ion and intergrid CEX collection current for beamlets that were near the extraction limit, as these ions are more effective agents of grid erosion than CEX ions formed in the downstream region. These ions typically impinge on the barrels at energies and angles of incidence that are more effective in generating sputter efflux per ion. Source gas in the intergrid region may collectively produce more sputtered atom density at grid center than downstream gas, despite much shorter collection length, due to elevated xenon density, more favorable angle of incidence, and higher average impingement energy. Variation of the relative magnitudes of these contributions underlies the molybdenum density profiles found across the grid face for DART throttle points.

Facility effects from background gas and carbon deposition on the grids were further elucidated. Background gas increases the apparent thruster erosion rate, whereas carbon deposition reduces it. To effectively model observed grid current levels and their dependence on propellant utilization and background pressure, it was necessary to increase the ratio of facility background to source flow gas density. This increase can make sense if background gas has directional bias and elevated average velocity. Hall thruster work has previously suggested a similar phenomenon, where the apparent ingestion of background gas was several times higher than predicted from gas density measurements at the test chamber wall and the assumed thermal velocity distribution. Average neutralization length was estimated based on the data modeling, helping to pin down this historically elusive figure.

Radial velocity bias of the sputtered molybdenum atoms was observed, increasing with the radial coordinate. Potential causes of this bias were discussed, but the ultimate origin is not certain. Implications with respect to site of origin and angular dependence of far-field flux were discussed.

Barrel erosion rate is typically higher for new grids, slowing down as the geometry changes. For situations where the spacecraft is highly sensitive to molybdenum deposition, the initial rate and deposit depth could be reduced by using grids with smaller gap, long break-in period, or otherwise modified geometry. This must be balanced against any negative performance effects.

Near-field molybdenum density and velocity measurements were calibrated with a single-point QCM flux measurement at 1-m distance, using an analytical model developed for this purpose. We then computed moly efflux rate on a 1-m arc from thrust axis, where the ion beam is far too intense for QCM measurements, to 36 degrees inside the backflow region. Nonzero measured deposition rate in the backflow region and the difference between the model prediction and QCM profile suggests the QCM observed molybdenum flux behind the thruster; if so, it would be the first such detection. Backflow may be enhanced by the radial velocity bias and ionized atoms whose trajectories are turned by the local electric field; the latter is not considered by the model.

Grid manufacturing methods and tolerances, as well as design and operating hours, influence behavior as illustrated by the present study. Ion engines should be treated as complex systems, with interacting extraction grids, discharge chamber, facility, and operating conditions, and behavior that changes over time.

Molybdenum LIF is a powerful tool to investigate the erosion process of ion engine grids. Due to the many factors involved, the data raise new questions as they answer old ones. A purpose-built extraction grid set, having annuli with independent voltage control and current collection, combined with molybdenum and xenon neutral profile measurements and the latest 3D particle-based codes for data modeling, could further elucidate the complex erosion process and lead to extraction grid performance that is properly optimized for a given spacecraft and its target mission.

Author Contributions: M.W.C. collected the data, analyzed and interpreted results, and wrote most of the manuscript; D.T.S. analyzed data and wrote Section 3.3; J.A.Y. wrote data acquisition and control software; M.J.P. operated the thruster, kept a detailed operations log, provided background information, and participated in technical discussions. All authors have read and agreed to the published version of the manuscript.

Funding: The original study and 2019 reports were funded by NASA Glenn Research Center, contract number NNJ11HB94C.

Data Availability Statement: Data available from MWC upon reasonable request. Use mwcrofton@outlook.com after January 2023.

Acknowledgments: Technical support was provided by Kevin McCormick, Mike Worshum, and Byron Zeigler. Vince Bilardo provided project management support, with assistance from Rostislav Spektor and Tom Curtiss.

Conflicts of Interest: The authors declare no conflict of interest. The funders had no role in the design of the study; in the collection, analyses, or interpretation of data; in the writing of the manuscript, or in the decision to publish the results. Technical personnel from the funding organization, especially MJP, did participate in determining the scope and work plan for the study, and helped with other aspects of the project.

References

1. Witze, A. NASA spacecraft will slam into asteroid in first planetary-defence test. *Nature* **2021**, *600*, 17–18. [CrossRef]
2. Rivkin, A.S.; Chabot, N.L.; Stickle, A.M.; Thomas, C.A.; Richardson, D.C.; Barnouin, O.; Fahnestock, E.G.; Ernst, C.M.; Cheng, A.F.; Chesley, S.; et al. The Double Asteroid Redirection Test (DART): Planetary Defense Investigations and Requirements. *Planet. Sci. J.* **2021**, *2*, 173. [CrossRef]
3. Shastry, R.; Herman, D.A.; Soulas, G.C.; Patterson, M.J. End-of-test Performance and Wear Characterization of NASA's Evolutionary Xenon Thruster (NEXT) Long-Duration Test, Paper AIAA-2014-3617. In Proceedings of the 50th AIAA/ASME/SAE/ASEE Joint Propulsion Conference, Cleveland, OH, USA, 28–30 July 2014.
4. Patterson, M.J.; Soulas, G.C.; Young, J.A.; Crofton, M.W. Expanded Throttling Capabilities of the NEXT Thruster, Paper AIAA-2013-3891. In Proceedings of the 49th Joint Propulsion Conference, San Jose, CA, USA, 14–17 July 2013.

5. Goebel, D.M.; Katz, I. *Fundamentals of Electric Propulsion*; John Wiley & Sons: Hoboken, NJ, USA, 22 December 2008.
6. Crofton, M.W.; Nocerino, J.C.; Young, J.A.; Patterson, M.J. NEXT Ion Engine Plume Deposition Rates: QCM Measurements, Paper AIAA-2014-0140. In Proceedings of the 52nd Aerospace Sciences Meeting, SciTech, National Harbor, MD, USA, 13–17 January 2014.
7. Crofton, M.W.; Patterson, M.J. Molybdenum LIF and NEXT Erosion Rate, Paper IEPC-2015-183/ISTS-2015-b-183. In Proceedings of the 34th International Electric Propulsion Conference, Hyogo-Kobe, Japan, 4–10 July 2015.
8. Ho, C.-S.; Banerjee, S.; Koel, B.E.; Duchemin, O.B.; Polk, J.E. Desorption of Chemisorbed Carbon on Mo(100) by Noble Gas Ion Sputtering: Validation of Ground Test Measurements of Ion Engine Lifetimes. *Appl. Surf. Sci.* **2006**, *252*, 2657–2664. [CrossRef]
9. Soulas, G.C. The Impact of Back-Sputtered Carbon on the Accelerator Grid Wear Rates of the NEXT and NSTAR Ion Thrusters, Paper IEPC-2013-157. In Proceedings of the 33rd International Electric Propulsion Conference, Washington, DC, USA, 6–10 October 2013.
10. Crofton, M.W.; Schoeffler, D.; Young, J.A.; Patterson, M.J.; John, J. LIF Erosion Rate Measurements of NEXT Ion Engine for DART Mission, Paper AIAA-2019-1246. In Proceedings of the AIAA SciTech Forum, San Diego, CA, USA, 7–11 January 2019.
11. Pollard, J.E.; Diamant, K.D.; Crofton, M.W.; Patterson, M.J.; Soulas, G.C. Spatially-Resolved Beam Current and Charge-State Distributions for the NEXT Ion Engine, Paper AIAA-2010-6779. In Proceedings of the 46th Joint Propulsion Conference, Nashville, TN, USA, 25–28 July 2010.
12. Miller, J.S.; Pullins, S.H.; Levandier, D.J.; Chiu, Y.; Dressler, R. Xenon Charge Exchange Cross Sections for Electrostatic Thruster Models. *J. Appl. Phys.* **2002**, *91*, 984–991. [CrossRef]
13. Thompson, M.W. Physical Mechanisms of Sputtering. *Phys. Rep.* **1981**, *69*, 335. [CrossRef]
14. Goehlich, A.; Rowekamp, M.; Dobele, H.F. Determination of the Velocity Distribution of Sputtered Atomic Oxygen by Laser-Induced Fluorescence in the Vacuum-Ultraviolet (130 nm). *Surf. Sci.* **1991**, *248*, 271–275. [CrossRef]
15. Crofton, M.W.; Murray, J.C.; Pollard, J.E. Xe+-Sputtered Molybdenum Properties at Low Impingement Energy, Paper IEPC-2005-194. In Proceedings of the 29th International Electric Propulsion Conference, Princeton, NJ, USA, 31 October–4 November 2005.
16. Farnell, C.C.; Williams, J.D.; Wilbur, P.J. NEXT Ion Optics Simulation via FFX, Paper AIAA-2003-4869. In Proceedings of the 39th Joint Propulsion Conference, Huntsville, AL, USA, 20–23 July 2003.
17. Diamant, K.D.; Liang, R.; Corey, R.L. The Effect of Background Pressure on SPT-100 Hall Thruster Performance, Paper AIAA-2014-3710. In Proceedings of the 50th Joint Propulsion Conference, Cleveland, OH, USA, 28–30 July 2014.
18. Ito, G.; Kawashima, R.; Komurasaki, K.; Koizumi, H. Study of Xenon Wall Accommodation Model and Background Flow during Hall Thruster Ground Test, Paper IEPC-2019-235. In Proceedings of the 36th International Electric Propulsion Conference, Vienna, Austria, 15–20 September 2019.
19. Frieman, J.D.; Liu, T.M.; Walker, M.L.R. Background Flow Model of Hall Thruster Neutral Ingestion. *J. Propuls. Power* **2017**, *33*, 1–15. [CrossRef]
20. Emhoff, J.W.; Boyd, I.D.; Shepard, S.P. Numerical Analysis of NEXT Ion Thruster Optics, Paper IEPC-03-110. In Proceedings of the 28th International Electric Propulsion Conference, Toulouse, France, 17 March 2003.
21. Varoutis, S.; Valougeorgis, D.; Sazhin, O.; Sharipov, F. Rarefied Gas Flow through Short Tubes into Vacuum. *J. Vac. Sci. Tech. A* **2008**, *26*, 228–238. [CrossRef]
22. Lu, C.; Zhang, T.; Qui, P.; Chen, J.; Cao, Y.; Zheng, L. Barrel Erosion of Ion Thruster Accelerator Grid under Different Operating Conditions. *IEEE Trans. Plasma Sci.* **2018**, *46*, 4065–4077. [CrossRef]
23. Boyd, I.D.; Crofton, M.W. Grid Erosion Analysis of the T5 Ion Thruster, Paper AIAA-2001-3781. In Proceedings of the 37th Joint Propulsion Conference, Salt Lake City, UT, USA, 8–11 July 2001.
24. Samanta Roy, R.I.; Hastings, D.E.; Gatsonis, N.A. Ion-Thruster Plume Modeling for Backflow Contamination. *J. Spacecr. Rocket.* **1996**, *33*, 525–534.
25. Polk, J.E.; Chaplin, V.; Yim, J.; Soulas, G.; Williams, G.; Shastry, R. Modeling Ion Optics Erosion in the NEXT Ion Thruster using the CEX2D and CEX3D Codes, Paper IEPC-2019-907. In Proceedings of the 36th International Electric Propulsion Conference, Vienna, Austria, 15–20 September 2019.
26. Emhoff, J.W.; Boyd, I.D. A Numerical Study of Neutralization and Sputtering Processes in the NSTAR Thruster, Paper AIAA-2002-4259. In Proceedings of the 38th AIAA/ASME/SAE/ASEE Joint Propulsion Conference and Exhibit, Indianapolis, IN, USA, 7–10 July 2002.
27. Brophy, J.R.; Katz, I.; Polk, J.E.; Anderson, J.R. Numerical Simulations of Ion Thruster Accelerator Grid Erosion, Paper AIAA-2002-4261. In Proceedings of the 38th AIAA/ASME/SAE/ASEE Joint Propulsion Conference and Exhibit, Indianapolis, IN, USA, 7–10 July 2002.
28. Soulas, G.C. Design and Performance of 40 cm Ion Optics, Paper IEPC-01-090. In Proceedings of the 27th International Electric Propulsion Conference, Pasadena, CA, USA, 15–19 October 2001.
29. Sengupta, A.; Goebel, D.; Owens, A. Neutral Density Measurements in an NSTAR Ion Thruster, Paper AIAA-2006-4491. In Proceedings of the 42nd Joint Propulsion Conference, Sacramento, CA, USA, 9–12 July 2006.
30. Bechtel, R.T. Effect of Neutralizer Position on Accelerator Wear for a 30-Centimeter Diameter Ion Bombardment Thruster. *NASA TM X-67926*; 1971; NASA Technical Reports Server (NTRS). Available online: ntrs.nasa.gov/citations/19710026638 (accessed on 29 July 2022).

31. Tartz, M.; Heyn, T.; Bundesmann, C.; Zimmermann, C.; Neumann, H. Sputter Yields of Mo, Ti, W, Al, Ag under Xenon Ion Incidence. *Eur. Phys. J. D* **2011**, *61*, 587–592. [CrossRef]
32. Thomas, R.E.; Patterson, M.J.; Young, J.A.; Crofton, M.W.; Foster, J.E. Advancements in the Demonstration of High Thrust to Power Ion Engine Technology, Paper AIAA-2015-3918. In Proceedings of the 51st Joint Propulsion Conference, Orlando, FL, USA, 27–29 July 2015. See Figure 7.
33. Shagayda, A.; Nikitin, V.; Tomilin, D. Three-dimensional Analysis of Ion Optics with Misalignments of Apertures. *Vacuum* **2016**, *123*, 140–150. [CrossRef]